Modeling of Casting, Welding, and Advanced Solidification Processes - XII
Edited by: Steve L. Cockcroft and Daan M. Maijer
TMS (The Minerals, Metals & Materials Society), 2009

New Insights into the Electro-Slag Remelting Process using Mathematical Modeling

Ashish D. Patel[1] and Kanchan M. Kelkar[2]

[1]Ashish D. Patel
Carpenter Technology, Corp, 101 W Bern St, Reading PA 19601, USA

[2]Kanchan M. Kelkar, Ph. D
Innovative Research, Inc., 3025 Harbor Lane N., Suite 300 Plymouth, MN 55447, USA

Keywords: Modeling, ESR, Pool-profile

Abstract

A mathematical model was developed to simulate the ESR process for cylindrical ingots. Typical results from this model which include current and joule heat distribution, temperature and flow field in the process are presented here. The model also predicts metallurgical parameters of interest like solidification time, cooling rate and the Rayleigh number. Inputs to the model include geometrical parameters like electrode and ingot diameter, slag height, and melting parameters like current, melt rate, power. Other inputs include slag & alloy properties and heat transfer coefficients. The effect of melting power and electrode & ingot diameter on the predicted flow and temperature within the process is examined. Model predictions are compared against experimentally measured pool shape from a 0.432 m diameter ESR ingot. Simulations were also conducted for different alloys using the identical melting parameters.

Introduction

There is renewed interest in modeling the Electro-Slag Remelting (ESR) process as evidenced by the surge in publication in the past few years /1-9/. This recent spike in activity is in part due to the need for such a tool in the specialty metal processing industry for new process development and optimization of existing melting parameters. The basic mathematical description of the ESR process was developed in the 80's /10, 11/. Most of the recent efforts have essentially adopted the same formulation, embedded within commercially available CFD codes. These days commercial CFD models are widely used within this industry as these codes are robust, have user friendly interfaces for pre and post processing, and the developers provide web based technical support. Also, the advent of faster computers has significantly reduced the run times for these process models.

A sketch of the ESR process is shown in Figure 1-A, typically in this process AC current is applied and the energy necessary to melt the electrode is generated by joule heating from the slag, whose resistivity is three orders of magnitude higher than that of the molten metal. There are a few variants of the ESR process, in the static mold process, the entire solidifying ingot is contained within the copper mold, where as in either the moving mold or the ingot withdrawal process, only a part of the ingot is contained within the short mold, and the remaining ingot is exposed to the atmosphere.

In this paper, typical results from ESR modeling using COMPACT-ESR™ will be illustrated /12/. The details of formulation, including the governing equations, boundary conditions, and

the numerical algorithm is discussed elsewhere, and is not discussed here /13/. The model performs a comprehensive analysis of the process for axi-symmetric, steady-state conditions using control volume technique for both static and moving mold ESR. A frame of reference attached to the top of the slag is used for the analysis so that the solidified ingot moves at the casting velocity through the computational grid as show in Fig 1-B.

The time-averaged electromagnetic behavior for applied current is governed by the magnetic diffusion equation. The magnetic field, in turn, determines the distributions of Lorentz forces in the slag and the molten pool, and the Joule heating in the slag. The turbulent flow field in the slag and the metal pool, created by the Lorentz and buoyancy forces, are analyzed by solving the time-averaged Navier-Stokes equations. The two-equation k-ε model is used to model the nonuniform turbulent mixing in the slag and the molten pool. The temperature fields in the slag and the ingot are governed by the energy conservation equation. As the metal droplets fall through the slag, they absorb heat from the slag. The loss of heat from the slag to the mold accounts for the presence of slag skin on the surface and considers the effect of the gradual loss of contact of the ingot due to shrinkage. The resulting computational model differs from earlier studies in its completeness of the analysis of the flow and thermal interactions between the slag and the metal regions based on advanced turbulence model for accurate simulation of turbulent mixing and rigorous treatment of thermal boundary conditions at the mold. The computational model is available in the software program COMPACT-ESR^{TM} and is used for performing analysis of the ESR process of interest.

The main focus of this article is to provide insights into this process by showing salient results from this modeling effort using typical processing parameters used for remelting specialty alloys. The results of the electromagnetic field distribution, temperature and flow field presented here are for a 0.356 m diameter electrode being remelted into a 0.432 m diameter ingot using a 0.127 m slag height.

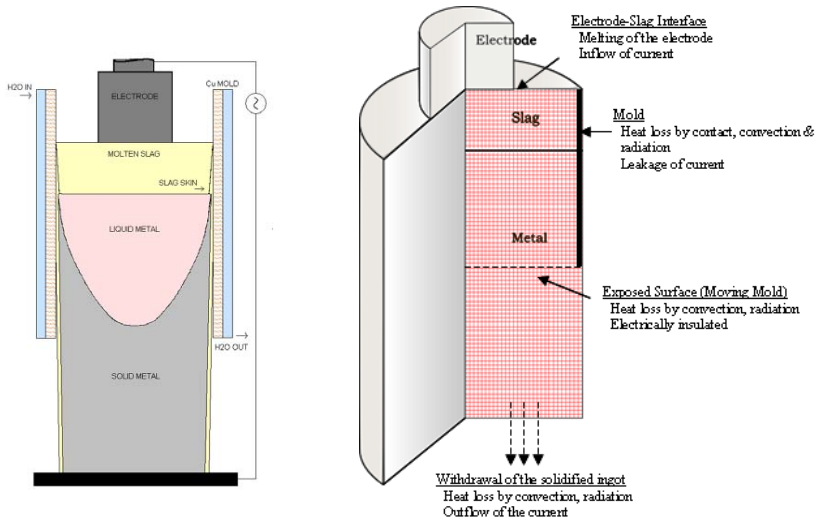

(A) (B)

Figure 1: Sketch of the Electro-Slag Remelting process (A) and the 2-D axi-symmetric computational domain and boundary conditions at the interface and surface (B).

Modeling Results and Discussion

The electromagnetic field distribution in ESR is shown in Figure 3, and the computed results are consistent with those from an analytical model /7/. As the current enters from the electrode into the slag it diverges, due to a larger cross-sectional area and again redistributes as it enters the ingot due to smaller skin depth (~ 0.0762 m) in the ingot. This is clearly seen in the current density vectors shown in Fig 3-A. The current density within the slag is uniform expect at the surface of the electrode, where as in the ingot, it decays from surface to the center, with a maximum of nearly $1x10^5$ A/m^2 at the surface. The computed magnetic field distribution is shown in Fig. 3-B, the maximum field is in the slag, in the vicinity of the edge of the electrode. The computed electrode magnetic force, which results from the interaction of the applied current with its associated magnetic field is shown in figure 3-C. The force field is predominantly in the radial direction, towards the symmetry axis. Due to the divergence of the current at the edge of the electrode, the force field is also large in this region of the slag, with a maximum of 500 N/m^3, under these operating conditions. The force in the metal, close to the slag-metal interface ranges from 300 N/m^3 at the surface to 5 N/m^3 at the center.

The calculated temperature distribution in the slag and within the entire ingot is shown in Figure 4-A. The joule heating in the slag under these conditions is nearly 247 kW, the maximum slag temperature is a few inches below the top surface, and is 1800^0 K, which is nearly 250^0 K above the slag liquidus. Under these conditions the pool is relatively shallow, with a depth of 0.127 m at the center. The flow in the slag is stronger than the molten pool as seen in Fig 4-B and 4-C.

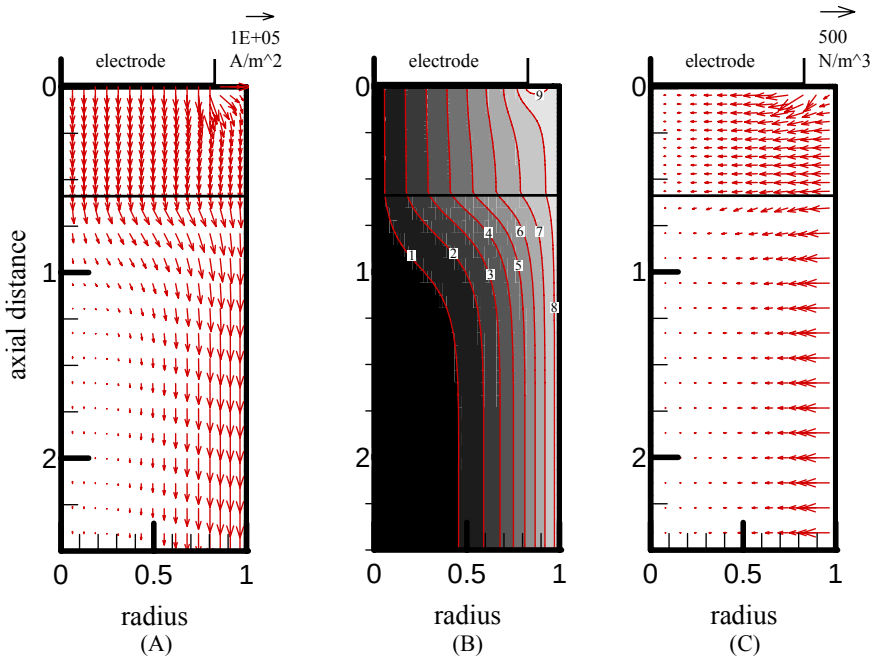

Figure 3: Calculated current density (A), magnetic field (B), and electromagnetic force (C). For the magnetic flux density, B field, there are 9 contours ranging from $5x10^{-4}$ T (contour 1) to $90x10^{-4}$ T (contour 9). The total applied current is 6.5 kA (rms), 60Hz. The axial and radial distances are normalized with respect to the ingot radius of 0.2159 m (8.5 inch).

In the slag, the computed flow shows two distinct loops, electromagnetic forces drive the flow in the counter-clockwise direction where as at the slag surface the clockwise flow is buoyancy driven. Whereas in the pool, the flow is buoyancy driven and is nearly an order of magnitude lower than that of the slag. The high values of the ratio of turbulent to molecular viscosity seen in Fig. 4-D indicate that the flow in the slag is highly turbulent, on the other hand, in the molten metal pool, the flow is nearly laminar and turbulence does not play a major role in heat distribution in the ingot.

Metallurgical parameters of interest like cooling rate, dendrite arm spacing and solidification time derived from the computed temperature distribution are shown in Figure 4-D. For a 0.4318 m diameter ESR ingot, the solidification time at the center is nearly 2500 Sec.

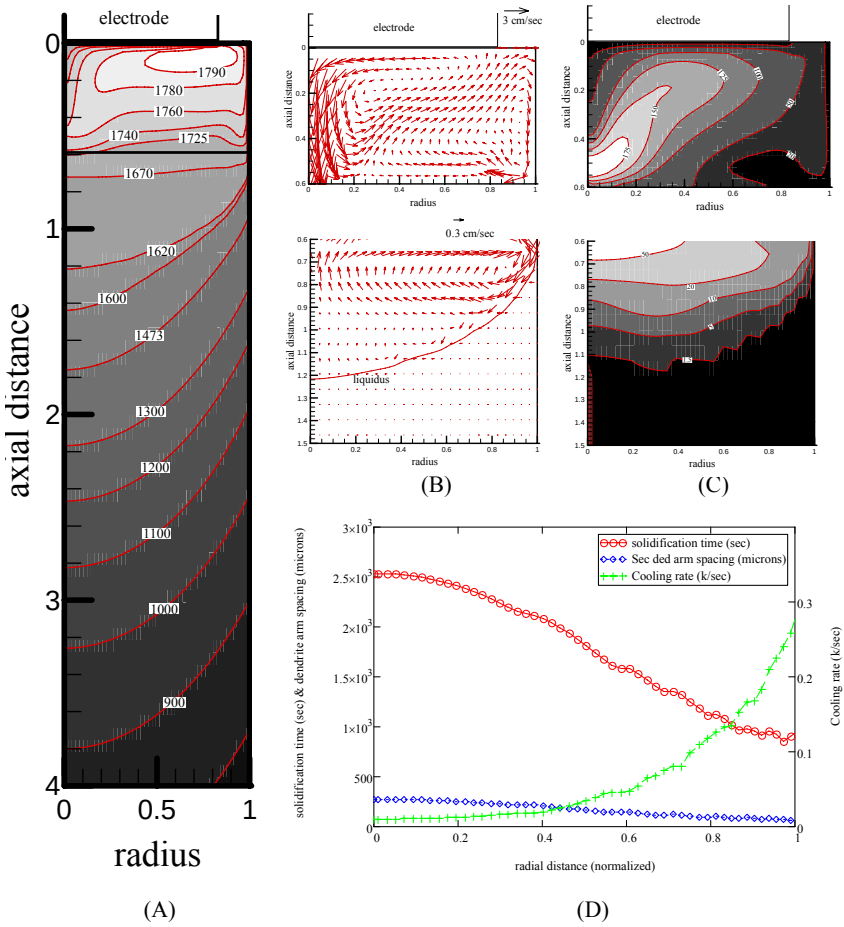

Figure 4: Computed results from the model for a 0.4318 m diameter ingot remelted at 6.5 kA. The steady state temperature distribution, in ^{0}K, within the slag and ingot (A), flow in the slag and molten metal pool (B), the ratio of turbulent to laminar viscosity (C) and other parameters of interest (D). Metal properties and 60/20/20 slag properties were obtained from literature /14-17/.

For model validation purposes, an industrial scale trial was planned on a 0.432 m diameter ESR ingot. Melting was interrupted by shutting off the power and a handful of nickel balls, nearly quarter inch diameter, were quickly introduced into the melt. Current was restored to a preset target value and melting resumed within a few minutes as shown in Fig. 5-C. The ingot was subsequently cut into longitudinal sections, with one face containing the ingot axis. The plates were ground, and conditioned prior to macro-etching using a ferric chloride solution and finally photographed. The marked pool profile is shown in Figure 5, owing to these processing conditions, the pool depth is nearly 0.127 m, and the entire pool profile (TL) is in reasonably good agreement with the model predictions shown in Fig. 5-A. The measured secondary dendrite arm spacing at the mid-radius and surface of the ingot was also within 10% of the predicted values from the model.

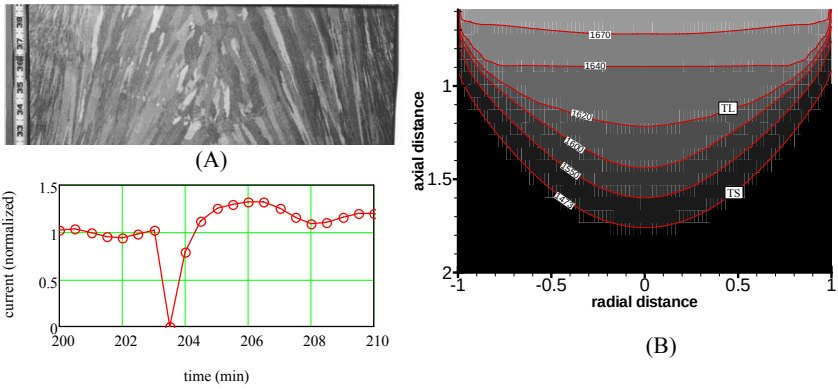

Figure 5: A comparison between the measured pool profile (A) and predicted (B) for a 0.4318 m diameter ESR ingot. Also shown in the current trace (C) during the melt interruption to mark the pool.

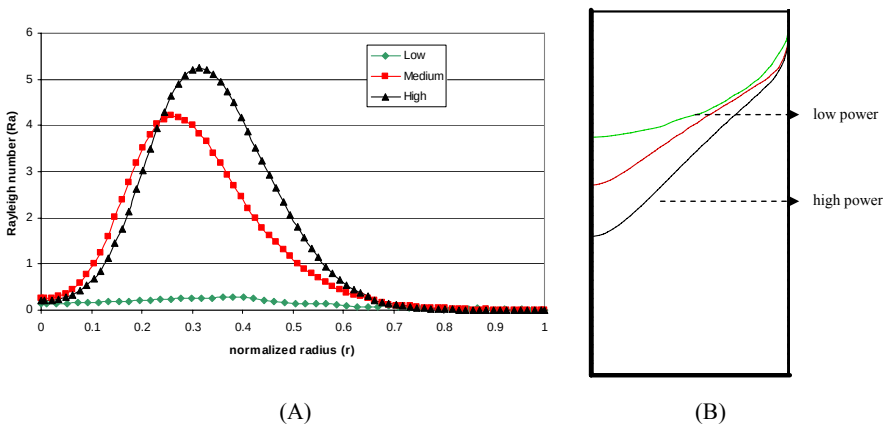

Figure 6: Effect of melt power on the predicted Rayleigh number at f_L=0.98 (A), and the change in pool profile with increasing power is shown on the right (B).

Another parameter of interest to process metallurgists is the dimensionless Rayleigh number, because beyond a critical value the likelihood defect formation in the cast ingot increases considerably /18/. At higher values of this number, the inter-dendritic flow in the mushy zone becomes unstable, and promotes channel formation by shearing the dendrites which manifests in a freckle type defect in the ingot. The predicted Rayleigh number is figure 6 increases with increasing pool power, and is maximum in between the center and mid-radius of the ingot. As power increase, the pool gets deeper and the slope of the liquidus isotherm increases. There is considerable debate on the critical Rayleigh number beyond which freckle originates; however, once the maximum threshold is determined the model does provide guidelines for the optimum operating window for the process.

In order to examine the effect of alloy properties on temperature field, simulations were conducted for iron and nickel based alloys using the same melting parameters, geometry, side wall boundary conditions and slag properties. Only the alloy properties were different, and these values were obtained from the commercial software package JMatPro /19/. Results shown in figure 7 clearly indicate larger solidification range for alloys 718 and A-286 compared to the steels. Another interesting prediction is that as the liquidus temperature decreases, the molten metal head at surface increases. This in turn decrease the contact resistance at the surface is, and hence heat losses from the ingot mold contact region are higher, resulting in a shallower pool, and a slightly lower slag temperature.

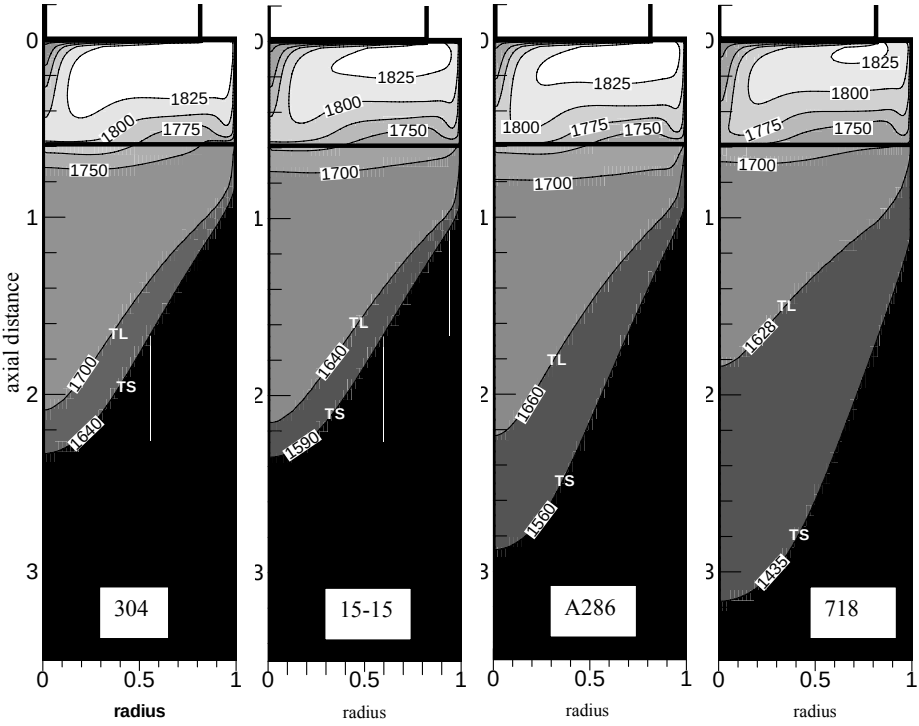

Figure 7: Computed ESR slag temperature (^{o}K) and pool profile for steels and high temperature alloys. The geometry, slag properties and operating parameters are identical in all four cases. Simulations were carried out at an operating current of 11 kA.

Simulations were also carried out to examine the effect of another key melting parameter, which is the diameter of the electrode to be remelted. Typically in a moving mold ESR process, the electrode diameter is lower than that of a static mold ESR process. Hence to illustrate these effects, simulations were carried out for a 0.508 m diameter ingot, processed using an electrode diameter of 0.356 m and 0.432 m, which represents a typical scenario for both moving mold and static mold ESR process. The slag height was held at 0.1524 m, and the current was also maintained at 11 kA in both cases. Simulations were carried out using thermo-physical properties of 304 stainless steel. Computed temperature distribution is shown in Figs. 8-A and 8-B. The slag temperature for the moving mold case is nearly 50^{o}K higher. The pool depth shown in Fig. 8-B is also higher, 0.365 m compared to 0.305 m for the static mold. The mushy zone size remains relatively the same in both cases at 0.05 m. The joule heat density is plotted in figures 8-C and 8-D. As the electrode diameter decreases, for the same current, the joule heat in the slag increases considerably. Under these conditions, the total heat generated in the slag is nearly 20% higher for the 0.356 m diameter electrode. The difference in the nature of the flow field in the slag and the pool is minimal in these two cases shown in Fig 8-A and 8-B. The flow field in the slag has two recalculating loops as described earlier.

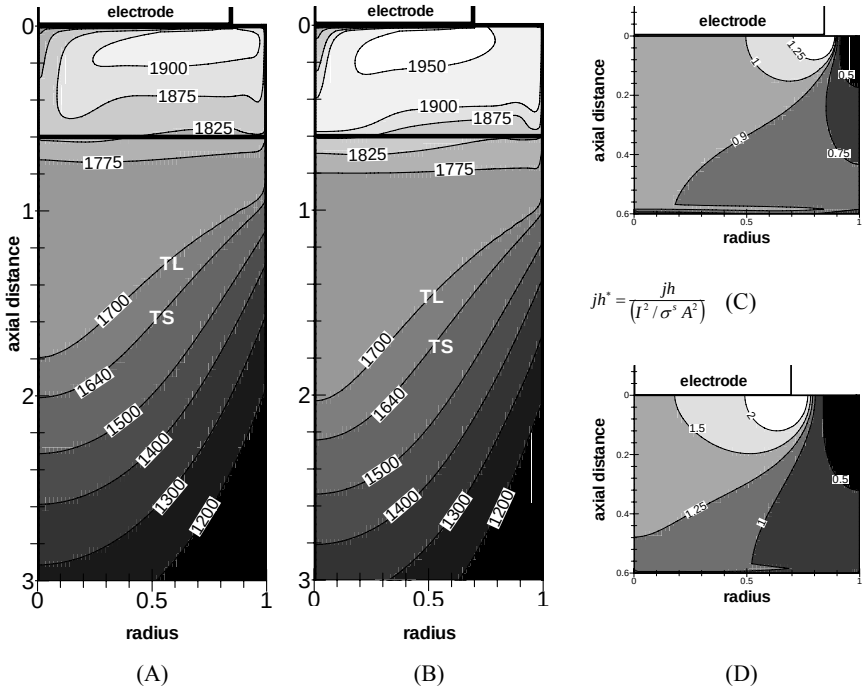

Figure 8: A comparison between the predicted temperature (^{o}K) distribution in static mold ESR (A) and moving mold ESR (B) for a 304 stainless steel ingot at the same current. The predicted joule heat density in the slag: static mold (C), and moving mold (D). The joule heat density is normalized with respect to the ratio of the square of the applied current density (I^2/A_i^2) to the electrical conductivity of the slag, σ^s.

Conclusion

A comprehensive model for the ESR process has been developed using a commercial CFD package, capable of predicting the electromagnetic field, flow, temperature distribution and metallurgical parameters that are of interest to process engineers in both moving mold and static mold processes. Analysis of the process using this model shows that the flow in slag is turbulent, driven by the strong electromagnetic forces, where as in the molted pool, the electromagnetic force is potential, and hence the flow is buoyancy driven and is weaker. The predicted Rayleigh number and solidification time are useful indicators for determining the upper bounds for key melting parameters. At lower power, the molten metal pool is shallow and shaped like a "bowl", and as the power input increases the pool becomes more "conical".

Acknowledgement

The author would like to thank Darin Tallman, Drexel University for assistance with characterization and post-processing as part of his summer internship at Carpenter

References

1. W. Schutzenhofer et al, Proc. Of Intl. Symp. On Liquid Metal Processing and Casting, ed. P. D. Lee et.al (SF2M, 2007) 49-54.
2. V. Weber et. al, Proc. Of Intl. Symp. On Liquid Metal Processing and Casting, ed. P. D. Lee et.al (SF2M, 2007) 83-88.
3. Z. Jiang and Y. Dong, Proc. Of Intl. Symp. On Liquid Metal Processing and Casting, ed. P. D. Lee et.al (SF2M, 2007) 89-94
4. A. Kharicha et al, Proc. Of Intl. Symp. On Liquid Metal Processing and Casting, ed. P. D. Lee et.al (SF2M, 2007) 107-112
5. Y. Dong et al, Journal of Iron and Steel Research, 2007, Vol. 14(5), 7-12, 30.
6. A. Ruckert and H. Pfeifer, 16th Intl. Metallurgical and Materials Conference, ed. Hradec and Moravivi, (METAL 2007)
7. A. Patel, Proc. Of Intl. Symp. On Liquid Metal Processing and Casting, ed. P. D. Lee et.al (SF2M, 2007), 95-100.
8. K. M. Kelkar, et al, Proc. Of Intl. Symp. On Liquid Metal Processing and Casting, ed. P. D. Lee et.al (ASM, 2005) 137-144.
9. S. Viswanathan et. al, Proc. Of Intl. Symp. On Liquid Metal Processing and Casting, ed. P. D. Lee et.al (ASM, 2005) 145-154.
10. M. Choudhary and J. Szekely, ISS Transactions, Vol 3, 1983, 67-75.
11. B. Hernandez-Morales. and A. Mitchell, Ironmaking and Steelmaking, 1999 Vol 26, No 6, 423-38.
12. COMPACT-ESR – Theoretical background and Use, Innovative research, Inc., 3025 Harbor Lane N., Suite 300, Plymouth, MN 55447, www.inres.com
13. K. M. Kelkar et.al, Submitted for publication, Modeling and Simulation: Processing of Metallic Materials, ASM Handbook series, Vol 22.
14. P. N. Quested et al, Proc. of Intl. Symp. On Liquid Metal Processing and Casting, ed. A. Mitchell and P. Auburtin (VMD, 1997), 1-17.
15. K.C. Mills and B.J. Keene, *International Metals Reviews*, 1, 1981, 21-69.
16. Verein D Eisenhüttenleute, *Schlackenatlas,* Düsseldorf, Germany: Verlag Stahleisen M. B. H., 1981, 55, 267.
17. A. Mitchell and J. Cameron, Met. Trans., 2, 1971, 3361-66.
18. P. Auburtin et al, Met. Trans 2000, Vol 31B, 801-811.
19. http://www.thermotech.co.uk/